3D printable lightweight cementitious composites with incorporated waste glass aggregates and expanded microspheres – Rheological, thermal and mechanical properties

Karla Cuevas [a], Mehdi Chougan [b], Falk Martin [a], Seyed Hamidreza Ghaffar [b], Dietmar Stephan [a], Pawel Sikora [a, *]

[a] Building Materials and Construction Chemistry, Technische Universität, Berlin, Germany
[b] Department of Civil and Environmental Engineering, Brunel University, London, Uxbridge, Middlesex, UB8 3PH, United Kingdom

ABSTRACT

One of the fields in the construction industry where 3D printing of cementitious composites can play a significant role is associated with manufacturing of lightweight structures. Thanks to 3D printing, structural self-weight can be reduced by topology optimization of printed elements. Moreover, further decrements of self-weight and improvement of thermal insulating properties can be achieved by the mixture design and introduction of materials of low thermal conductivity. To date, limited knowledge on lightweight printable mixtures is available. The main objective of this study is to develop 3D printed lightweight concrete (3DPLWC) mixture, with the intention of replacing natural aggregate with waste glass (WG) by 50 vol.-% and 100 vol.-%. Moreover, expanded thermoplastic microspheres (ETM) were incorporated into the mixture. This led to a reduction in density of the mixtures as well as the thermal conductivity by up to 40%. Comprehensive evaluation of material's fresh properties revealed that the addition of ETM results in 3D printable material with lower yield shear stress and higher plastic viscosity by 28% and 66%, respectively, compared to the mixes without ETM. Moreover, improvement of shape retention, flowability, setting times, and early-hardened mixtures' properties was observed. The mechanical properties of 3DPLWC showed that the replacement of natural aggregate by 50 vol.-% WG led to enhanced flexural and compressive strength of the composite, while full replacement resulted in retaining or slight reduction of the mechanical properties.

1. Introduction

3D printing of concrete (3DPC) has gained particular momentum in recent years with substantial development of the printing techniques, mixtures designs as well as first practical large-scale applications. Additive manufacturing of concrete offers many advantages, including geometrical freedom as well as formwork-less concreting [1]. Although there are substantial developments in this field, there is still concern related to cost optimization of the 3DPC mixtures [2,3]. To ensure proper printing parameters (mainly flowability and buildability), mixtures dedicated for printing consist of the high volume of fine fractions and admixtures which in turn results in the increment of the final cost of the printed element. Therefore, various solutions are sought to meet this challenge. This can be achieved both by replacing either the binder with various supplementary cementitious materials (SCMs) or fillers as well as replacing natural aggregates [2,4,5]. Skibicki et al. [6] showed

that cement can be successfully replaced with a high content of limestone filler without deteriorating the printing properties of the mixtures, thus producing more sustainable mixtures. Similarly, Panda et al. [7] introduced high-volume fly ash mixtures for 3D printing. Moreover, to mitigate the problem with shortages of natural sand resources, various approaches including production of mixtures with sea sand [8,9] or copper tailings [10,11] were proposed. Zou et al. [12] replaced the natural river sand with recycled sand from construction and demolitions waste (C&DW). However, it was found that incorporation of recycled sand requires additional mixture modifications as recycled sand noticeably affects the workability of the fresh mixture [13]. A study by Xiao et al. [14] showed that the replacement of sand with recycled sand by 25 wt.-% caused higher green strength of specimens compared to control with no apparent effects on mechanical performances of specimens. Zou et al. [12] reported that it is possible to produce printable material with 100% recycled sand; however, an acceptable extrudability and a

suitable printability window for practical printing required the intro-duction of retarding admixture of sodium gluconate.

Ting et al. [15] evaluated the possibility of incorporating recycled (waste) glass aggregate for 3D concrete printing. Waste glass (WG) with a grain size of up to 1.7 mm was incorporated into the mixture. The mixture with recycled glass exhibited lower dynamic yield stress and plastic viscosity than the control mixture with river sand. This indicates that the mixture with recycled glass demonstrates a better flowability. On the contrary, lower static yield stress for the mixture with WG was reported, resulting in weaker buildability of the mixture during print-ing. In addition, the authors reported substantially lower compressive, flexural, and tensile strengths of mixtures with WG. However, it is worth mentioning that waste glass has good potentials to be used for in-sulating mortars and concretes. Studies [16,17] showed that cement mortars produced with fine WG aggregate exhibited only one-third of the thermal conductivity of mortars containing standard quartz aggre-gate. Similarly, Chung et al. [18] demonstrated that WG aggregate with a particle size up to 4 mm could be successfully used to produce light-weight concretes with satisfactory mechanical and thermal properties.

To date, many valuable research works were performed towards de-veloping normal-weight cement-based and alkali-activated 3D printed concrete mixtures, while limited efforts have been focused to produce lightweight printable mixtures for thermal insulating applications. Mo-hammad et al. [19] performed a study on the production of lightweight printable mixtures with expanded perlite (up to 4 mm) used as sand re-placement in 3DPC. Replacement of sand with perlite aggregates re-sulted in the decrement of thermal conductivity of 3DPC by 62%. How-ever, along with unit weight decrement the flexural and compressive strength reduction was reported. Markin et al. [20] developed three dif-ferent foamed concrete printable mixtures with oven-dry densities ranging between 970 and 1307 kg/m³ and compressive strength above 10 MPa. Rahul and Santhanam [21] evaluated the printability of con-cretes containing 15, 30, and 45 vol.-% of natural sand substitutions with coarse expanded clay aggregates (up to 4 mm). Extrudability tests showed that lightweight aggregate could be incorporated into the mix-ture up to 30 vol.-% of replacement. A higher volume of aggregates re-sulted in liquid phase separation in the piston pump. Wang et al. [22] evaluated the mechanical behaviors of 3D printed lightweight concrete structures with hollow sections. Fine sand has been replaced up to 30 wt.-% with ceramsite sand to decrease the density of the elements. Structures with different topologies were evaluated showing the promising approach for using 3D printing technology for such a pur-pose. Zhou et al. [23] suggested that the density of printable mixtures can be successfully decreased by incorporating various lightweight fillers (such as hollow glass microspheres or fly ash cenospheres). Much smaller particle size than that of aggregate and mostly spherical shape enables controlling rheological properties. Moreover, even a small dosage can lead to a noticeable decrement of unit weight due to ex-tremely low density. Therefore, based on the literature review, it can be seen that knowledge related to the production of printable lightweight mixtures is still not broad and most of the available studies are limited to particular properties such as printability properties or mechanical performance. Hence there is no comprehensive study dedicated to de-veloping 3D printable lightweight cementitious composites.

The main objective of this work is to develop a 3D printed light-weight concrete (3DPLWC) mixture, towards improving the thermal in-sulating characteristics of 3DPLWC. Waste glass aggregates (WG) and expanded thermoplastic microspheres (ETM) were incorporated into the mixture. Comprehensive evaluations of rheological, thermal, and mechanical properties of the composite were conducted. Key parame-ters governing the material rheology, thermal and mechanical behav-iour are assessed and discussed.

2. Materials and mixture design

2.1. Materials

To produce specimens, a binder composed of CEM III 42.5 N (Ce-mex, Germany) and limestone powder (Opterra, Germany) with spe-cific gravities of 3.0 g/cm³ and 2.7 g/cm³, respectively, were utilized in all mixtures. As an aggregate, basalt crushed aggregate (Baden-Württemberg, Germany) with a specific gravity of 2.96 g/cm³ was in-corporated into the mixture. Brown soda-lime beverage glass obtained from a local recycling company was used as a source of waste glass (WG) aggregate. Crushed glass cullets with broad particle size distribu-tion were washed, dried, milled and sieved to pass the sieve of 1 mm. The specific gravity of the WG aggregate is 2.53 g/cm³. Fig. 1 presents the particle size distribution of dry materials obtained by laser diffrac-tion particle size analyzer Mastersizer2000 (Malvern Panalytical Ltd., UK). Limestone filler was found to be finer than the cement particles with D50 of 9.4 μm when compared to D50 of cement, which is 17.5 μm. Basalt aggregate showed a narrow grain distribution with D50 of 474 μm, while the distribution of glass particles was broader due to the milling process required to prepare the aggregate. Scanning elec-tron microscopy (SEM, Zeiss GeminiSEM500 NanoVP) study of aggre-gate particles (Fig. 2) confirmed that WG preparation process results in presence of large amount of flat, elongated and needle-shaped glass particles (Fig. 2(b-d)).

Additionally, Sika PerFin 300 (Sika Deutschland GmbH, Germany) defoaming admixture, a modified aqueous polyol solution with a den-sity of 0.96 g/cm³ was used. To suppress the shrinkage of mixtures, dis-persed basalt fibres with an average length of 6 mm produced by the Deutsche Basaltfaser GmbH (Germany) were used in the mixture. The density of the fibres was 2.96 g/cm³.

To decrease the density of mixtures, pre-wetted expanded thermo-plastic microspheres (ETM) Expancel 461 WE 20d 36 (Nouryon AB, Sweden) with a true density of 36 ± 4 kg/m³ were used. This material is an inert material, traditionally used as a lightweight filler and a blow-ing agent [24,25]. Microspheres' estimated particle size equal to D50 of 20–30 μm (data provided by the supplier). Size distribution was addi-tionally confirmed by laser granulometry study (Fig. 1), while SEM study confirmed the spherical morphology and narrow particle size dis-tribution of spheres is presented in Fig. 2(e–f).

2.2. Mixture design

Table 1 presents the six 3D printable mixtures designed for the ex-perimental program. Mixture compositions were developed through se-ries of initial trials with the principle of fixed cement content. Mixes G0, G50, and G100 are normal-weight mixtures, while mixes G0-ETM, G50-ETM, and G100-ETM were designed to be light-weight mixtures with the addition of 3 wt.-% (by mass of binder) of ETM. G0 and G0-
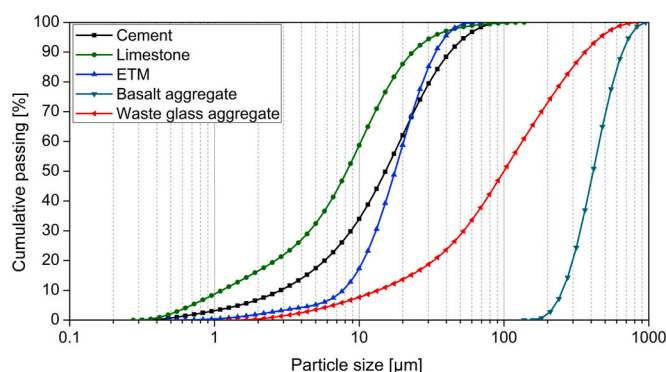
Fig. 1. Particle size distribution of cement, limestone, expanded thermoplastic microspheres, basalt and waste glass aggregates.
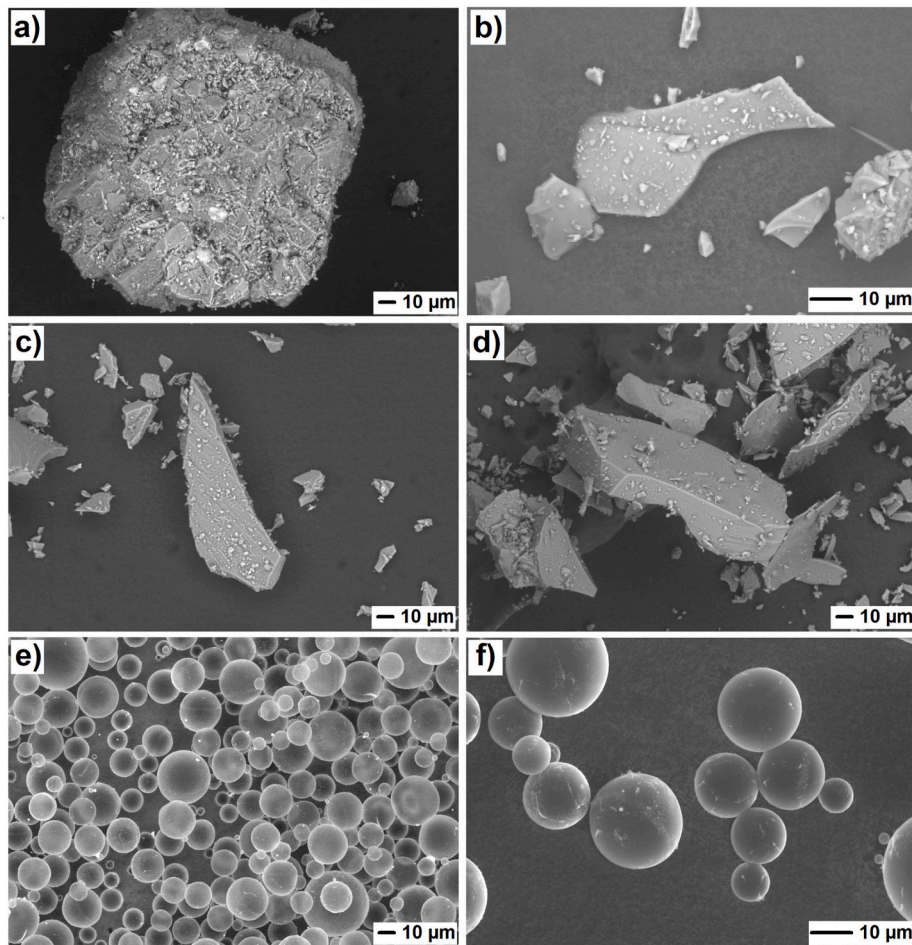
Fig. 2. SEM micrographs of basalt aggregate (a), waste glass aggregate (b–d) and expanded microspheres (e–f).

Table 1
Mass-related mixing ratio.

Mix designation	Binder	Water	Expanded microspheres	Basalt aggregate	Waste glass aggregate	PerFin 350 [%][c]	Fibres [%][c]
G0	1[a]	0.35	0	0.44	0	0.7	0.3
G50	1[b]	0.37	0	0.22	0.22	0.7	0.3
G100	1[b]	0.38	0	0	0.44	0.7	0.3
G0-ETM	1[a]	0.37	0.03	0.44	0	0.7	0.3
G50-ETM	1[b]	0.38	0.03	0.22	0.22	0.7	0.3
G100-ETM	1[b]	0.39	0.03	0	0.44	0.7	0.3

[a] Cement:limestone ratio 1:0.52.
[b] Cement:limestone ratio 1:0.49.
[c] By weight of binder.

ETM are considered as control mixtures with 100 vol.-% of basalt aggregate. In G50 and G50-ETM mixes, basalt aggregate was replaced with waste glass by 50 vol.-%, while in G50 and G50-ETM mixes, basalt aggregate was entirely replaced with WG (i.e. 100 vol.-%).

The water-to-binder ratio (w/b) ranged between 0.35 and 0.39 and the aggregate-to-binder (a/b) was 0.44 in all samples. Replacement of basalt aggregate with waste glass required a slight increment of water and decrement of limestone from the binder phase due to higher finesses of waste glass, thus higher water absorption. Moreover, in the case of ETM incorporation, a slight increment of water was also required to meet the consistency required for the mixture to be printed. The consistency, similar to other studies [6,26,27], was determined using a flow-table method (conforming EN 1015–3) with a targeted flow between 135 and 165 mm. The content of Perfin 350 admixture and fibres was fixed to 0.7% and 0.3% by mass of binder, respectively.

2.3. Mixing and printing process

The mixing procedure of printable composites was performed using a standard rotary mixer conforming to EN 196–1 [28]. Firstly dry components were mixed for 1 min, and then water and admixtures were added followed by a second mixing phase of 1 min at 140 rpm. The third mixing phase consisted of high-speed mixing (285 rpm) for 1 min. Afterwards, the mixture was left for 1 min to rest and mixed again for 1 min at high speed. Thereafter, the mixture was poured into $40 \times 40 \times 160$ mm^3 prismatic mould to produce the casted samples. After 24 h, the casted specimens were demolded and tested or immersed in water up to 7 d, 14 d and 28 d, depending on the testing date.

The printer used in this study is an XYZ-gantry system equipped with an active pumping nozzle for composite displacement developed

by TU Berlin. The different mixture compositions were all printed with the following printer properties:

- a nozzle diameter of 6 mm,
- a print path of 10 mm width and 2.5 mm height,
- printing time of one prism 7 min (average volume flow of 600 cm³/s),
- printing speed 0–40 mm/s (according to 0–1000 mm³/s),
- pausing of composite displacement after every layer, restarting new layer according to the print path shown in Fig. 3.

A set of prismatic specimens (40 × 40 × 160 mm³) were printed to evaluate shape retention, mechanical and thermal properties. Fig. 3 represents a schematic four-layer repeatable printing path obtained from a previously developed G-code. The printed object is also represented in this (Fig. 4). After printing, the samples were inserted in a compartment containing a humidifier (T = 20 ± 5 °C, 99% RH) to cure the samples for 24 h to prevent shrinkage. After 24 h, the samples were immersed in water to replicate the curing method for casted samples.

3. Testing procedures

3.1. Determination of fresh properties

To evaluate the fresh properties of developed mixtures following tests were performed:
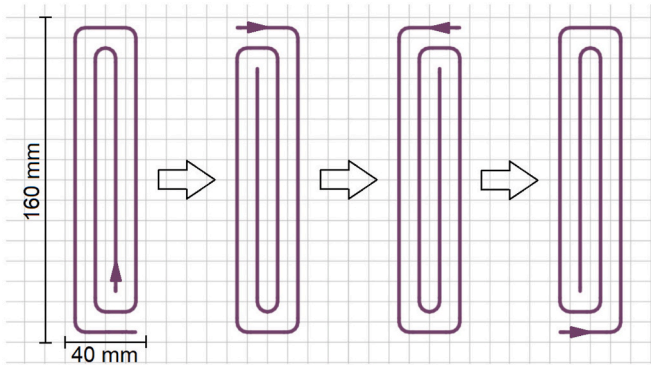
- Flow table test measurement conforming to EN 1015-3 [29] was performed at 0, 5, 10, 15, 30, and 60 min, where time 0 corresponds to the flowability 5 min after the addition of water to the mixture.
- Two different methods have been conducted to evaluate the setting behaviour of the mixtures. The automatic penetrometer Toni Technik ToniSET Force (Zwick Roell, Germany) conforming ASTM C403 was employed to determine the penetration resistance of fresh mixture over time. The yield stress obtained from the data collected by the penetrometer was calculated using the proposed method by Wünsch [30]. The measurements stopped when the force reached 400 N at two speeds of 0.03 mm/min and 0.072 mm/min. Additionally, a Vicat needle test conforming EN 196–3 [31], using an automated Toni Technik ToniSET (Zwick Roell, Germany) was performed to determine the initial and final setting times of the fresh mixtures.
- The rheology measurements were conducted by means of Viskomat NT (Schleibinger, Germany). The rheology test protocol based on Haist et al. [32] is presented in Fig. 5. The rheology testing protocol consists of a pre-shearing stage, where the shear rate increases rapidly from 15 s⁻¹ to 135 s⁻¹ for 1 min, followed by gradual decrements of 15 s intervals until the shear rate reaches 15 s⁻¹. Several fitting models [33–35], including the Modified-Bingham (MBM) and Herschel-Bulkley (HB) models, have been reported to calculate the rheological parameters of the mixtures. However, based on some of the authors' previous studies [36,37], due to the non-Newtonian and pseudoplastic nature of the OPC-based cementitious composites, as well as increasing the fitting accuracy, the Modified-Bingham model was employed to extract the plastic viscosity (η_p), and yield shear stress (τ_o) of each mixture (see Eq. (1)).

$$\tau = \tau_0 + \eta_P.\gamma + C\gamma^2 \tag{Eq. 1}$$

where τ is the yield shear stress (Pa), η is the apparent viscosity (Pa.s) and γ is the shear rate (1/s).

- A mini-slump test, with cone dimensions of 19 mm top diameter, 38 mm bottom diameter and 57 mm height, was performed according to the model proposed by Tan et al. [38]. Based on slump data, the yield stress was calculated according to Ref. [38] with the use of Eq. (2).

$$\tau_0 = \frac{(225 * \rho g \Omega^2)}{128 * \pi^2 R^5} \tag{Eq. 2}$$

Fig. 3. Schematic presentation of four-repeatable printing patterns for prismatic specimens.
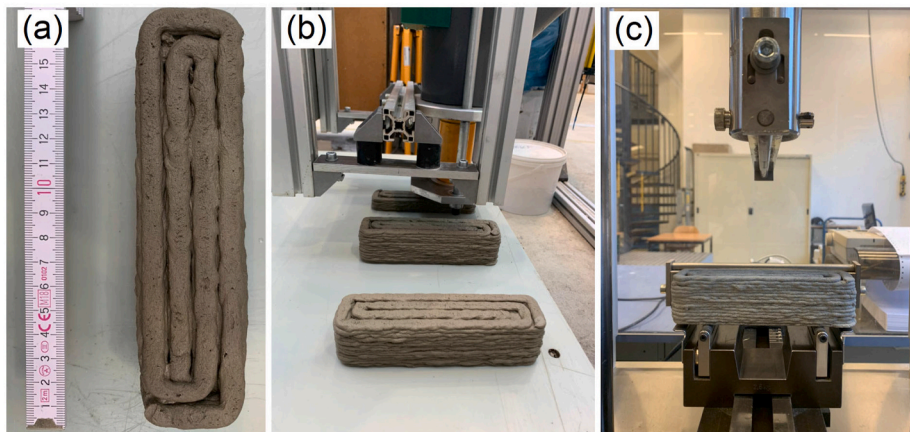

Fig. 4. Printing process of specimens (a) and (b) and flexural strength determination (c).
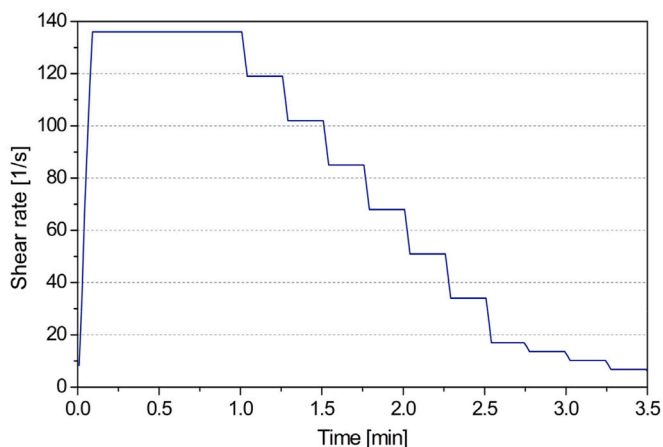
Fig. 5. Test program of rheological measurement procedure.

Fig. 6. Flowability of mixtures according to EN 1015-3.

where: τ_0 is the yield stress, ρ is the density of the paste, g is the gravitational acceleration, Ω is the volume of the mini-slump cone and R the mini-slump spread diameter.

- The shape stability or shape retention of each mixture was studied by comparing the height (H_1) of the first layer and the difference between the height of the first and the last printed layer (H_{dif}). Based on some of author's previous studies [35,39], samples were printed until reaching approximately 40 mm in height (16 layers). The first and the last deposited layer's height were measured by taking high-quality footage of the printed sample's front view and importing them to the ImageJ software for accurate analysis.

3.2. Thermal properties

Thermal conductivity, thermal diffusivity, and specific heat were measured using a Hot Disk TPS 2200 with a 6.4 mm Kapton-insulated sensor compatible with ISO 22007–2 [40]. Thermal properties were determined on both casted and printed prisms with dimensions of $40 \times 40 \times 160$ mm^3 after 28 d of curing. Prior to the measurement, the samples were dried until constant mass. Each mix design was tested on three groups of specimens, with the mean value taken into consideration in each case.

3.3. Evaluation of mechanical properties

Compressive and flexural strength testing was performed on casted and printed prisms at ages 1 d, 7 d, and 14 d with dimensions of $40 \times 40 \times 160$ mm^3 according to EN 196–1 [28]. A batch of three prisms for each composition was initially tested for flexural strength in the perpendicular direction to the specimens' printing path. A total of six broken portions of prisms in flexural strength test were utilized for compressive strength evaluations. Prior to testing, the surface of the printed specimens was flattened with sandpaper to ensure proper testing conditions.

4. Results and discussion

4.1. Fresh properties

4.1.1. Flowability

The flowability of a cementitious composite is of particular importance in qualifying a good printable mixture. This parameter was tested using the flow table test according to the EN 1015–3 [29]. Fig. 6 presents the results of the flow table measurement. The spread-flow of each mixture was recorded for up to 60 min after the mixing process. The results indicate that all the combinations' flowability meets the adequate
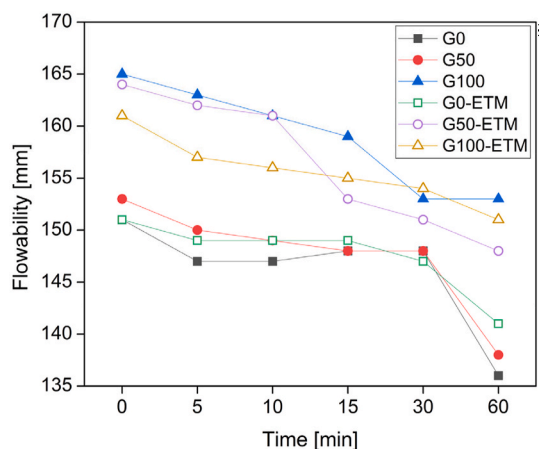
range (i.e. between 135 and 165 mm) to retain their shape after the printing process [3,26,27]. As can be seen, by increasing the WG replacement percentage, the initial and final flow of cementitious composites gradually increased from 151 mm to 136 mm for G0 (control sample) to 153 mm and 138 mm for G50 and 165 mm and 153 mm for G100. However, it should be taken into account that mixtures G50 and G100 required slight mix modification, including limestone filler reduction and increment of the water content, to meet the flowability range. Although it has been reported that WG particles have remarkably lower water absorption capacity [15], the presence of flat elongated and needle-shaped glass particles increases the internal friction in the mix [18]. Moreover, compared to basalt aggregate, WG aggregate was finer due to the milling process (Fig. 1), which led to an increase in the water absorption of the material.

The results also show that the incorporation of ETM has a remarkable impact on altering the flowability trend. Even though a high-volume of ETM particles were incorporated into the G0-ETM, G50-ETM and, G100-ETM mixes, there was only marginal modification of mixture composition (minimal increment of water content) required when compared to the corresponding G0, G50 and G100 mixes. The initial and final flow of G0-ETM (i.e. 151 mm and 141 mm, respectively) and G50-ETM (i.e. 164 mm and 148 mm, respectively) increased compared to the values registered for the corresponding mixtures without ETM, i.e. G0 and G50, respectively. The result has to be associated with the fact that the addition of fine ETM particles affects the packing density of the mixtures. An increase in packing density results in a stiffer mix caused by reducing the water demand and consequently causes an overall higher flow when compared to samples without ETM particles. Another hypothesis is that the extra water from the pre-wetted ETM could increase the mixture's water content, resulting in an increased flowability. Moreover, the inclusion of microspheres with a spherical shape reduces the cohesiveness of the paste. The presence of spherical shape particles is expected to act as a lubricant, leading to an increased flowability [41–43]. Several other studies have also indicated that the presence of spherical particles leads to a reduction in frictional force between the mix's main components and act as a lubricant which results in a higher flowability [44,45]. On the contrary, the initial and final flowability of G100-ETM slightly decreased and reached 161 mm and 151 mm, which are lower than the values measured for G100 (i.e. 165 mm and 153 mm). One possible hypothesis for this effect is attributed to the agglomeration of ETM particles in this mixture. As indicated by Liu et al. [46] high volume of ETM particles might exhibit tendency to agglomeration, which could in turn affect slightly decrease the flowability of this particular mixture. All designed mixtures exhibited an appropriate flowability up to 60 min, and in all cases, loss of flowability did not exceed 9.2%.

4.1.2. Initial and final setting time

The initial and final setting times of the cementitious composites are presented in Fig. 7. The results indicate a noticeable delay in initial and final setting times for all the mixtures incorporated with ETM (i.e. G0-ETM, G0-ETM, and G0-ETM) compared to the corresponded combinations without microspheres (i.e. G0, G50, and G100). This is attributed to the non-reactive (inert) character of ETM particles which does not exhibit any chemical affinity with binder phase [24,25]. The same relationship was also observed in the penetration resistance (PR) results (Fig. 8), in which, after 4 h, the PR of the samples containing ETM particles was considerably lower than the values registered for the mixtures without it. This proves that the aforementioned mixtures will reach final setting slower. As previously mentioned (see section 4.1.1), a relatively small amount of excess water entrapped in the pre-wetted ETM spheres (i.e. increased w/c ratio) can also lengthen (i.e. increase both initial and final setting times) the setting process of the mixtures containing ETM [47].

For mixtures without ETM, it can be seen that (Fig. 7) by replacement of basalt with WG particles, the setting times (i.e. initial and final setting time) of the mixtures has reduced and reached 2.5 h and 4.1 h for G50, and 3.1 and 4.3 h for G100 compared to the values registered for G0 (i.e. initial and final setting times of 3.5 and 5.3 h, respectively). This observation can be attributed to the "filler effect" or "pozzolanic reaction" induced by replacing basalt particles with finer WG particles.
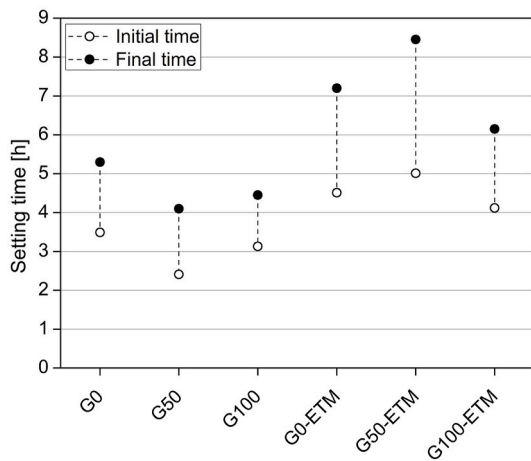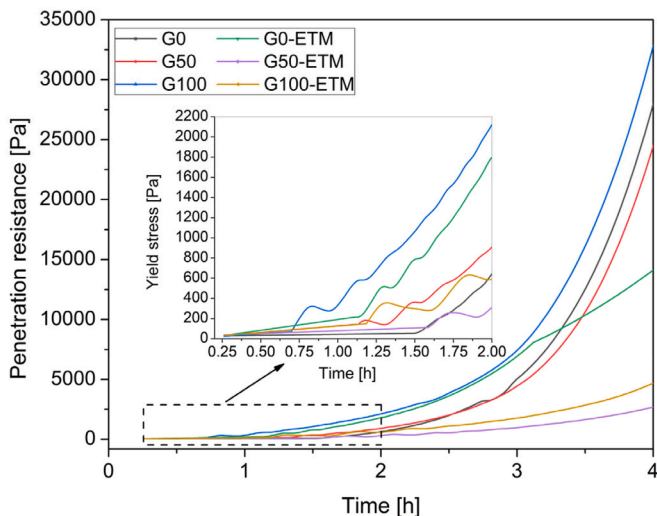
The aforementioned phenomena provide extra nucleation sites within the cementitious composite paste leading to an acceleration in the cement hydration kinetics [48]. The results indicate the ascending trend by increasing the replacement percentage as at 50 vol.-% replacement of basalt (i.e. G50), the setting time was lower than G100 (i.e. 100 vol.-% replacement). After the inclusion of ETM particles, the setting times were first increased to 5 h and 8.3 h for G50-ETM (i.e. 50 vol.-% replacement), which is higher than the initial and final setting time of G0-ETM (4.5 and 7.2 h, respectively). This can be attributed to a variation in the mixture compositions. As discussed in the previous section, Mix G50-ETM required a slight decrement of limestone filler content along with slight water content increment (Table 1) to meet the flowability requirements. This resulted in slightly lower contents of binding material as well as higher amount of free water available in the mixture. Thus the initial flow (Figure M1) of G50-ETM was 164 mm (the upper region of flowability requirement) compared to the G0-ETM flow of 151 mm. This resulted in elongation of the setting time of G50-ETM. Thereupon, for G100-ETM (i.e. 100 vol.-% replacement), the initial and final setting time decreased to 4.1 h and 6.1 h, respectively, due to higher content of fine WG particles as well as similar binder content as in case of G50-ETM.

4.1.3. Rheological properties

It is well accepted that suitable mixtures for 3D printing process should exhibit low yield stress and adequate flowability to facilitate the mixture's extrusion through the nozzle. Moreover, at the same time, the high viscosity is also required to guarantee the shape stability of the deposited layer immediately after printing [49]. Fig. 9 demonstrates the shear stress versus shear rate flow curves of each mixture. After fitting the Modified-Bingham model, yield stress and plastic viscosity of each mixture have been extracted. As shown in Fig. 10, the inclusion of spherical ETM particles is influential in changing the rheological behaviour of cementitious composites by decreasing the yield stress and recovering the plastic viscosity of the mixtures. Examining the mixtures' yield stress reveals that the yield stress of 712 Pa, 614 Pa, and 737 Pa was registered for G0, G50 and G100, respectively. However, after incorporating ETM particles, the yield shear stress was reduced to 585 Pa, 608 Pa, and 548 Pa for G0-ETM, G50-ETM and G100-ETM, respectively. Accordingly, the plastic viscosity of the G0 (i.e. 1.052 Pa s), G50 (i.e. 1.575 Pa s), and G100 (i.e. 1.672 Pa s) is remarkably increased to 1.750 Pa s, 1.975 Pa s, and 2.188 Pa s for G0-ETM, G50-ETM, and G100-ETM, respectively. One possible hypothesis explaining the effects on yield stress and plastic viscosity is attributed to the impact of particles' spherical shape, facilitating the transition of paste principle components when subjected to shear [50,51]. Fig. 10 shows each mix evaluated by the mini-slump test, where the same descending trend of mix-
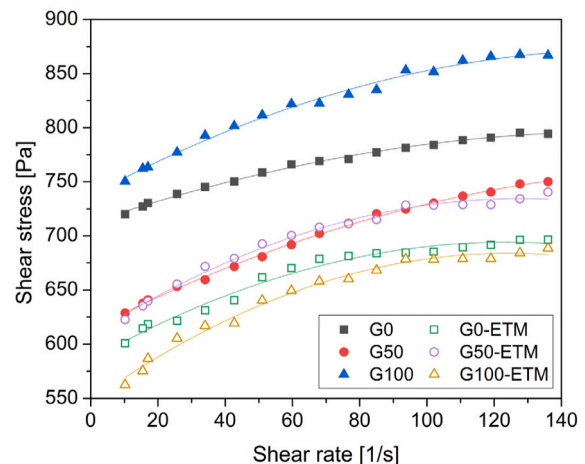

Fig. 7. Initial and final setting of mixtures.

Fig. 8. Penetration resistance between 15 min and 4 h obtained through a penetrometer test.

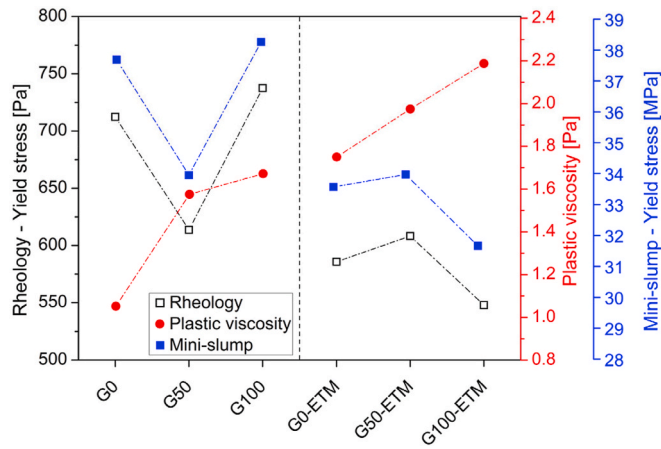**Fig. 9.** Shear stress of printable mixtures under a varying shear rate.

Fig. 10. Rheological parameters calculated through the rheology tests and mini-slump test.

ture's yield stress after the inclusion of ETM particles is observed. The lower yield stress of samples containing ETM could also be related to the higher setting time of these mixtures, which is indicated in Figs. 7 and 8.

4.1.4. Shape retention

The shape retention test was performed on the 3D printed mixtures to identify the shape stability of deposited layers that can be directly related to the rheological behaviour. This relation can be used to optimize the shape stability, buildability, and overall print quality of the printed specimen. Fig. 11 presents the sides of printed specimens while Fig. 12 shows the shape retention test results, where the first layer's height (H_1) and the difference between the height of the first and the last printed layer (H_{dif}) for each mix are presented. The results indicated the direct relation between H_1 and yield shear stress of mixtures. It was found that similar to the yield stress reduction, which is due to the ETM incorporation, the H_1 of the mixtures also decreased. The H_{dif} of mixtures, on the other hand, showed an inverse relation with plastic viscosity. The results indicated that the H_{dif} of G0 (i.e. 0.133 mm), G50 (i.e. 0.117 mm), and G100 (i.e 0.028 mm) was higher than their corresponding mixtures with ETM, by 14%, 62% and 53% for G0-ETM, G50-ETM and G100-ETM, respectively. The lower H_{dif} values for mixtures containing ETM comparing the corresponding mixtures without ETM suggest that the ETM inclusion can positively affect the critical printing parameters (i.e.

low yield stress and adequate plastic viscosity) and improve the final buildability of the printed objects.

4.2. Hardened properties

4.2.1. Thermal properties

Experimental results of thermal conductivity (TC) and specific heat of casted and printed specimens determined using a Hot Disk device are presented in Fig. 13. Noticeable differences between the casted and printed specimens can be distinguished. Printed specimens generally exhibited lower thermal conductivity and specific heat values attributed to the cavities and imperfections in the printed prisms which resulted in lower densities of specimens (Fig. 14) and higher deviation of the results (Fig. 13). The gradual replacement of basalt aggregate with WG aggregate resulted in a decrement in the thermal conductivity of the composites. Specimens G50 and G100 exhibited 11% and 17% (respectively) lower thermal conductivity than G0. Basalt aggregates are known to possess relatively low thermal conductivity compared to other commonly used aggregates e.g. siliceous aggregates [52]. It is worth noting that the thermal conductivity of soda-lime glass is over three times lower than that reported for a quartz aggregate [17]. However, the replacement of basalt with WG decreased the thermal conductivity of specimens by less than 20%.

The addition of ETM had a substantial contribution to the improvement of insulating properties of composites. As it is widely agreed, the density of the lightweight cement-based composites has a major effect on the thermal conductivity of composites [53–55]. G0-ETM, G50-ETM, and G100-ETM specimens exhibited 36%, 38%, and 40% lower thermal conductivity, respectively, when compared to G0. Similarly, the specific heat value of composites were decreased as a result of basalt aggregate replacement with WG by both 50 vol.-% and 100 vol.-%. The substantial improvement of thermal properties of ETM-modified specimens is attributed to the extremely low density of ETM particles (36 ± 4 kg/m^3); thus remarkable decrement of specimen's density was reported (Fig. 14). Therefore, in ETM-modified specimen, the effect of WG aggregate incorporation was limited.

4.2.2. Flexural strength

Results of flexural and compressive strengths of casted and printed specimens after 1 d, 7 d, 14 d and 28 d of curing are presented in Fig. 15 and Fig. 16, respectively. In general, the data show that the printed samples' flexural strength slightly increases or stays comparable in most of the samples at all curing ages. Similar observation were found in other studies with specimens tested in perpendicular direction to the printing path [56,57]. There are two potential reasons that can explain
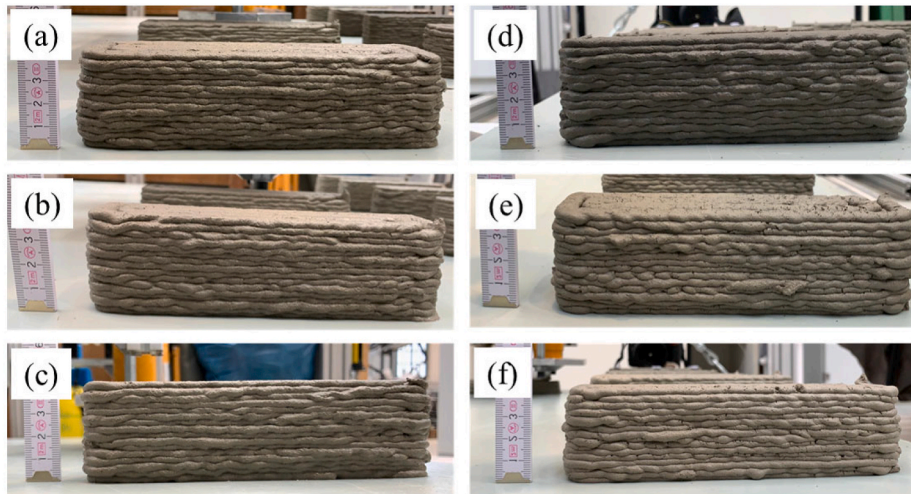

Fig. 11. Side view of the printed G0 (a), G50 (b), G100 (c), G0-ETM (d), G50-ETM (e) and G100-ETM (f).
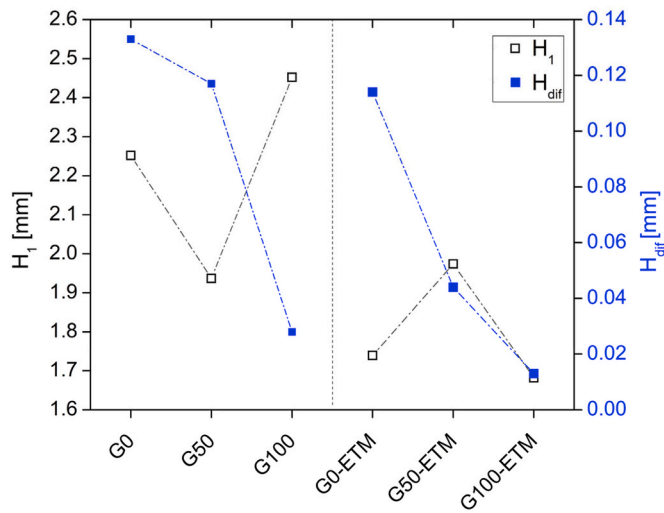
Fig. 12. Shape retention of the mixtures.

such results. Firstly, it could be attributed to minimal inconsistency with the printed specimens' dimensions, thus larger cross-section, which can slightly affect the measured values [58]. Secondly, as reported by Le at al [56]. due to printing process, there is a better com-

paction and local reduction of water-binder ratio in bottom layers. In this part of specimen the maximum tensile stress occurs, thus printed specimens exhibit higher flexural strength. Moreover, after 28 days of curing the discrepancy between the results of flexural strength of casted and printed specimens has decreased. This confirms faster hydration process of printed specimens as a result of exposed layers' surface during printing process and first hours of curing. Replacement of basalt aggregate with WG did not affect the flexural strength of casted specimens up to 28 d of curing. In case of printed specimens, a trend can be visible, indicating that mixtures containing 50 vol.-% of WG (G50 and G50-ETM) exhibit higher flexural strength values in all tested ages. This can be attributed to the orientation of elongated and angular glass particles (Fig. 2) along the printing paths, which occurs during the extrusion through the nozzle. Since force has been subjected in the perpendicular direction to the printing path, the fine oriented WG particles, introduced as a partial replacement of coarser basalt aggregate, improved the microstructure of the composite. In contrary, sole presence of WG in the composite (G100 and G100-ETM) resulted in comparable strength values to that of corresponding control mixes (G0 and G0-ETM). Recent study of Arunothayan et al. [57] confirmed that the printing process influences the fiber orientation, thus printed specimens exhibited greater alignment in the printing direction than the casted specimens.

The addition of ETM particles to the mixtures resulted in significant reduction of flexural strength. After one day of curing, printed G0-ETM, G50-ETM, and G100-ETM exhibited 55%, 51%, and 48% lower flexural
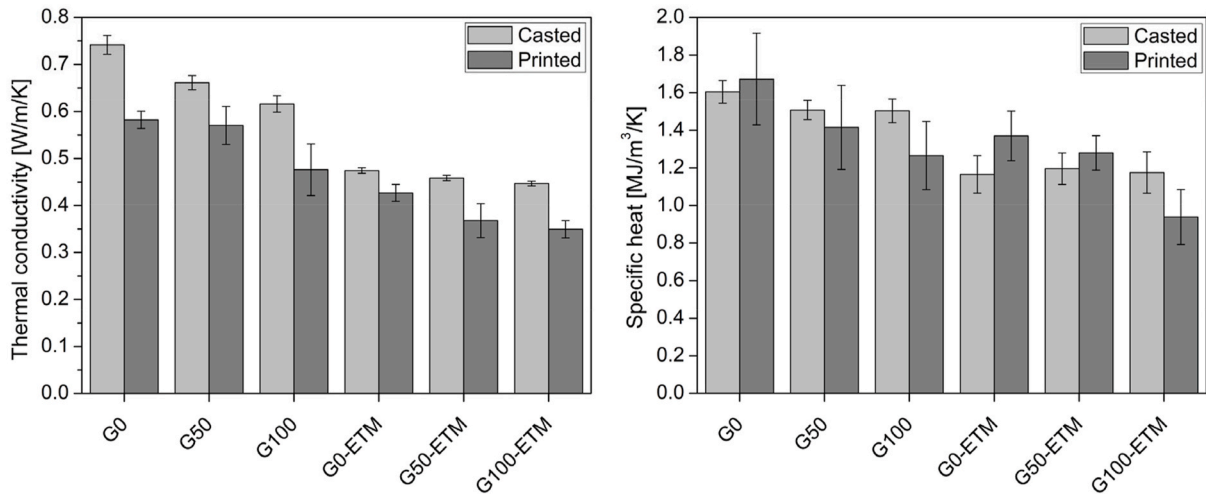

Fig. 13. Thermal conductivity (left) and specific heat (right) of specimens after 28 d of curing.
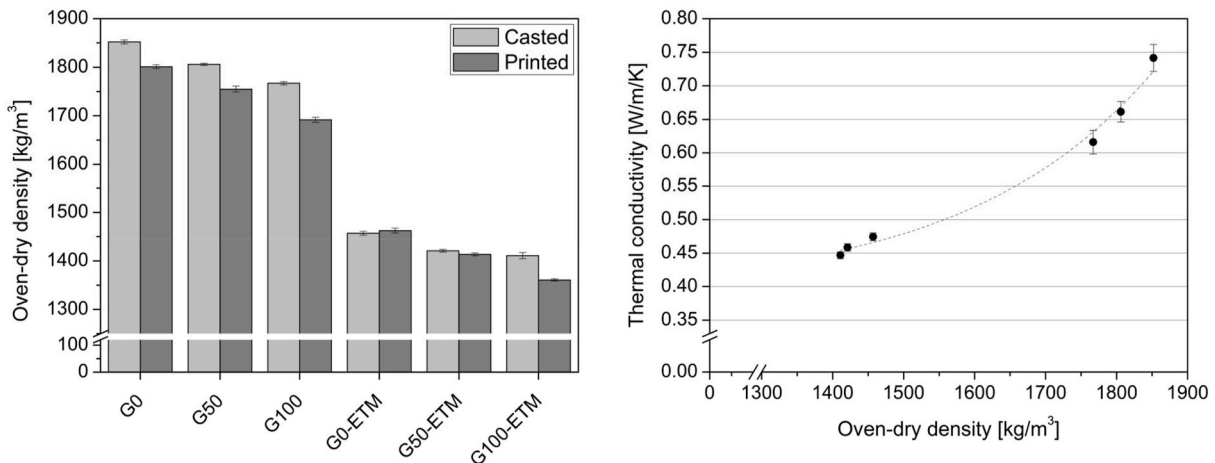

Fig. 14. Oven-dry densities of casted and printed specimens (left) and thermal conductivity of casted specimens tested through Transient Plane Source (TPS) method as a function of oven-dry density (right).
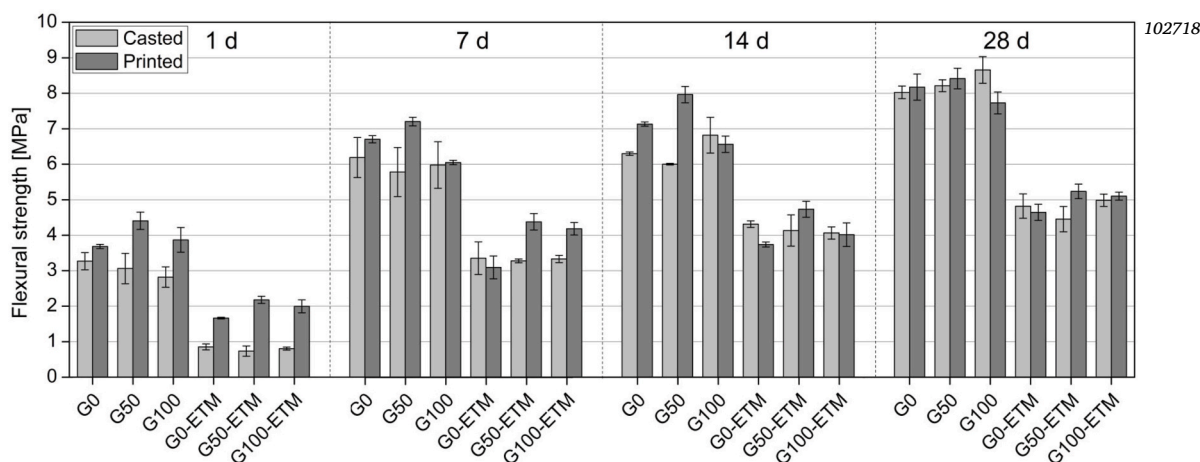
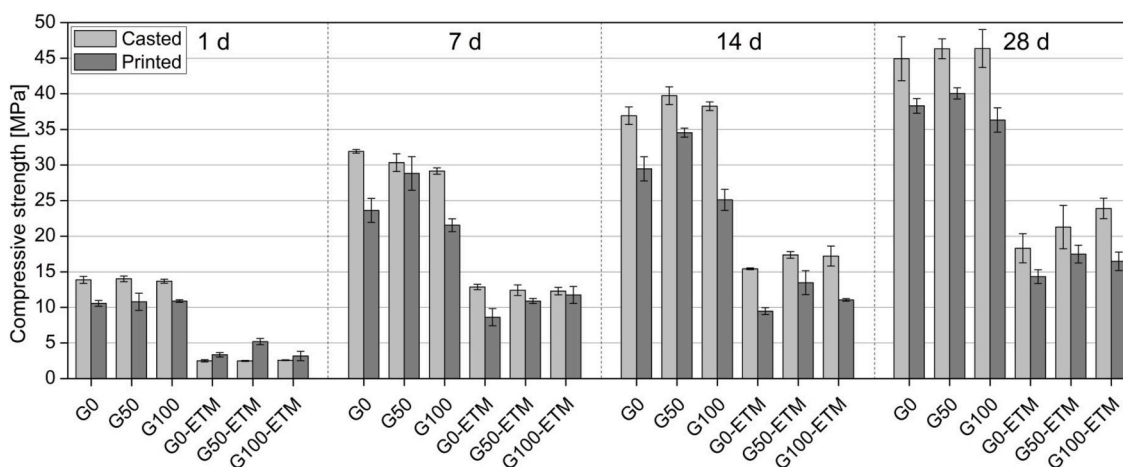**Fig. 15.** Flexural strength of casted and printed specimens after 1 d, 7 d, 14 d and 28 d of curing.

Fig. 16. Compressive strength of casted and printed specimens after 1 d, 7 d, 14 d and 28 d of curing.

strength than corresponding G0, G50, and G100 specimens, respectively. Along with the curing time, the discrepancy between flexural strength of specimens has been reduced. Hence after 14 days of curing, printed samples containing ETM (i.e. G0-ETM, G50-ETM and G100-ETM), exhibited approximately 47%, 40%, and 38% lower flexural strength than corresponding G0, G50, and G100 specimens, respectively. The results indicate that the flexural strength of samples without ETM drastically increased in the first seven days of curing and the improvement was gradual up to 28 days. While, for the samples modified with ETM, the mixtures experienced a gradual increase from 1 day to 28 days of curing. This has to be associated with the ability of ETM spheres to decelerate the hydration kinetics of the mixtures [25].

4.2.3. Compressive strength

Compressive strength results of casted and printed specimens show a higher discrepancy with printed specimens exhibiting lower strength values. After one day of curing, both groups of tested mixtures (i.e. with and without ETM) exhibited comparable compressive strength values in corresponding groups. After 7 d and 14 d of curing, noticeable differences between specimens can be distinguished. Printed G50 specimens showed improved compressive strength by 22% and 17%, respectively, compared to G0. In contrary, compressive strength of printed G100 declined by 8% and 15%, respectively when compared to G0. After 28 days of curing similar trend has been observed. Thus printed specimens exhibited lower strengths than casted. Lower compressive strength values of printed specimens can be attributed to small imperfections (voids) in the prisms produced with the unidirectional printing pattern.

As reported by Ma et al. [59] and Pham et al. [60] such printing pattern can result in certain anisotropy of the mechanical strength of specimens and have an adverse effect on the specimens' strength.

The replacement of basalt aggregate with 50 vol.-% of WG seems to be the most effective for improving mechanical properties of printable composite, while full aggregate replacement resulted in strength reductions. This can be attributed to the inclusion of finer WG particles which has improved the packing ability of coarser crushed basalt aggregate. As discussed briefly in previous sections, the finesses and geometrical characteristics of WG exhibit filling ability, increasing the internal friction and interlocking mechanism resulting in improved mechanical performance of the composites [61–63]. However, there is still no agreement in literature to what extent incorporation of WG is beneficial for improving the mechanical performance of composites. Several studies related to conventional cement-based composites have reported deterioration of flexural and compressive strengths when normal-weight aggregate is replaced with WG [64–67], while other works reported either beneficial or negligible effects of WG on mechanical behaviour of composites [18,62,68–70]. Similarly, Ting et al. [15] reported significantly lower mechanical performance of 3D printed concrete when fine river sand was replaced with WG (< 1.7 mm). There are two main factors responsible for such discrepancy in the literature. Firstly, the particle size of crushed aggregate plays a vital role in mechanical enhancement. In general, it is well accepted that coarser glass particles are more prone to cracking and exhibiting lower mechanical resistance [71,72]. Second aspect is related to the reference aggregate, which is used for comparison purposes. Since aggregates usually occupy between 60% and 80%

of volume of cementitious composites, their mechanical performance plays a crucial role in the overall mortar and concrete characteristics [73,74]. Therefore, the nature of aggregate, its geometrical characteristics, as well as gradation, are of high importance. For instance, siliceous and carbonaceous aggregates possess lower mechanical properties than, crushed basalt aggregate, which is considered high-quality aggregate due to its high density and high mechanical strength [74,75]. Therefore, our study showed that WG is a suitable solution compared to basalt aggregate, especially when used as partial replacement (i.e. up to 50 vol.-%).

The incorporation of ETM resulted in a substantial reduction in compressive strength of specimens. This can be attributed to the significant density reduction because of ETM presence. The density of lightweight concrete (< 2000 kg/m^3 [76]) is a major factor affecting the compressive strength [77,78], thus with the reduction of density, the compressive strength is also reduced. After one day, printed G0-ETM, G50-ETM, and G100-ETM exhibited 68%, 48%, and 70%, respectively, lower compressive strength than corresponding specimens without ETM. Similar trend was observed for samples after 14 days, in which compressive strength values remained lower by 68%, 60%, and 56% compared to that of corresponding specimens. An additional reason for the compressive strength reduction, could be the mitigation of hydration process due to the inert nature of ETM particles, which was also reflected in the retardation of mixtures setting times (see section 4.1.2). This was reflected in the slower strength gain in ETM-modified specimens compared to corresponding mixtures without ETM. Comparable strength losses were reported by other researchers [24,25,79] for conventionally cast cement-based composites modified with lightweight fillers. In the case of ETM-modified specimens both WG replacement dosages showed positive effects on the compressive strength of 3DPLWC. Printed G50-ETM and G100-ETM exhibited higher compressive strength by 42% and 17%, respectively after 14 days of curing, while after 28 d printed G50-ETM and G100-ETM exhibited 22% and 15% higher than G0-ETM.

5. Conclusions

This study was aimed to develop a 3D printed lightweight concrete (3DPLWC) with incorporated waste glass aggregates. The following conclusions can be put forward:

- Waste glass (WG) as well as expanded thermoplastic microspheres (ETM) can be successfully used to produce 3DPLWC, however, minor mixture composition modifications are required to replace conventional (basalt aggregate) with WG up to 100 vol.-% to satisfy the flowability requirements of 3D printing process.
- Incorporation of fine WG aggregate results in shortening of the initial and final setting times of printable composites. Addition of ETM, due its inert nature, results in retardation of mixtures setting times. Nevertheless, delay in setting time of 3DPLWC was partially compensated by incorporation of higher amount of WG.
- The inclusion of ETM can lead to improved final buildability of the printed objects by modifying the rheological behaviour of mixtures. For ETM-modified mixtures (i.e. G0-ETM, G50-ETM, and G100-ETM), the yield stress was reduced by 18%, 1%, and 26%, respectively. Moreover, the plastic viscosity was increased by 66%, 25%, and 31%, respectively, compared to the fresh mixture without ETM (i.e. G0, G50, and G100, respectively).
- After incorporating ETM spheres, G50-ETM shows the most preferable shape retention as it retains its first layers height, while difference between the height of its first and last printed layer (H_{dif}) decreased by 62% compared to the corresponding sample without ETM (i.e. G50).
- Replacement of basalt aggregate with WG aggregate by 50 vol-% and 100 vol.-% resulted in reduction of composites' thermal conductivity by 11% and 17%, respectively. While, addition of ETM

to mixtures significantly reduced composites' density which led to remarkable improvement of thermal insulation properties. 3DPLWC mixtures containing WG aggregate (50 vol.-% and 100 vol.-%) and ETM exhibited, respectively, 38% and 40% lower thermal conductivity when compared to control mix G0.
- Replacement of basalt aggregate with WG aggregate by 50 vol-% (G50) improved the flexural and compressive strength of composite, while mixtures containing 100 vol.-% (G100) experienced a decline in the compressive strength of printed composite. In contrary for both G50-ETM and G100-ETM, an improvement of mechanical properties was observed.

Authors contributions

Karla Cuevas: Methodology, Validation, Formal analysis, Investigation, Writing - Original Draft, Writing - Review & Editing. **Mehdi Chougan:** Methodology, Software, Validation, Formal analysis, Data Curation, Writing - Original Draft, Writing - Review & Editing, Visualization. **Falk Martin:** Investigation. **Seyed Hamidreza Ghaffar:** Software, Validation, Writing - Review & Editing. **Dietmar Stephan:** Resources, Supervision, Project administration, Funding acquisition, Writing - Review & Editing. **Pawel Sikora:** Conceptualization, Methodology, Validation, Formal analysis, Data curation, Investigation, Writing - Original Draft, Writing - Review & Editing, Project administration, Funding acquisition.

Declaration of competing interest

The authors declare that they have no known competing financial interests or personal relationships that could have appeared to influence the work reported in this paper.

References

[1] S. Ghaffar, P. Mullett, Commentary: 3D printing set to transform the construction industry, Proceedings of the Institution of Civil Engineers - Structures and Buildings, 171, 2018, pp. 737–738, https://doi.org/10.1680/jstbu.18.00136.

[2] P. Sikora, M. Chougan, K. Cuevas, M. Liebscher, V. Mechtcherine, S.H. Ghaffar, M. Liard, D. Lootens, P. Krivenko, M. Sanytsky, D. Stephan, The effects of nano- and micro-sized additives on 3D printable cementitious and alkali-activated composites: a review, Appl. Nanosci. (2021), https://doi.org/10.1007/s13204-021-01738-2.

[3] M. Kaszyńska, S. Skibicki, M. Hoffmann, 3D concrete printing for sustainable construction, Energies 13 (2020) 6351, https://doi.org/10.3390/en13236351.

[4] M.-I. Álvarez-Fernández, M.-B. Prendes-Gero, C. González-Nicieza, D.-J. Guerrero-Miguel, J.E. Martínez-Martínez, Optimum mix design for 3D concrete printing using mining tailings: a case study in Spain, Sustainability 13 (2021) 1568, https://doi.org/10.3390/su13031568.

[5] P. Sikora, S.-Y. Chung, M. Liard, D. Lootens, T. Dorn, P.H. Kamm, D. Stephan, M. Abd Elrahman, The effects of nanosilica on the fresh and hardened properties of 3D printable mortars, Construct. Build. Mater. 281 (2021) 122574, https://doi.org/10.1016/j.conbuildmat.2021.122574.

[6] S. Skibicki, M. Kaszyńska, N. Wahib, M. Techman, K. Federowicz, A. Zieliński, T. Wróblewski, N. Olczyk, M. Hoffmann, Properties of composite modified with limestone powder for 3D concrete printing, in: F.P. Bos, S.S. Lucas, R.J.M. Wolfs, T. A.M. Salet (Eds.), Second RILEM International Conference on Concrete and Digital Fabrication, Springer International Publishing, Cham, 2020, pp. 125–134.

[7] B. Panda, S. Ruan, C. Unluer, M.J. Tan, Improving the 3D printability of high volume fly ash mixtures via the use of nano attapulgite clay, Compos. B Eng. 165

(2019) 75–83, https://doi.org/10.1016/j.compositesb.2018.11.109.

[8] L.G. Li, B.F. Xiao, Z.Q. Fang, Z. Xiong, S.H. Chu, A.K.H. Kwan, Feasibility of glass/basalt fiber reinforced seawater coral sand mortar for 3D printing, Additive Manufacturing (2020) 101684, https://doi.org/10.1016/j.addma.2020.101684.

[9] A.V. Sharanova, A.O. Tovpinets, M.A. Dmitrieva, Application of sea sand for 3D concrete printing, IOP Conf. Ser. Mater. Sci. Eng. 597 (2019) 12033, https://doi.org/10.1088/1757-899X/597/1/012033.

[10] G. Ma, Z. Li, L. Wang, Printable properties of cementitious material containing copper tailings for extrusion based 3D printing, Construct. Build. Mater. 162 (2018) 613–627, https://doi.org/10.1016/j.conbuildmat.2017.12.051.

[11] G. Ma, J. Sun, L. Wang, F. Aslani, M. Liu, Electromagnetic and microwave absorbing properties of cementitious composite for 3D printing containing waste copper solids, Cement Concr. Compos. 94 (2018) 215–225, https://doi.org/10.1016/j.cemconcomp.2018.09.005.

[12] S. Zou, J. Xiao, T. Ding, Z. Duan, Q. Zhang, Printability and advantages of 3D printing mortar with 100% recycled sand, Construct. Build. Mater. (2020) 121699, https://doi.org/10.1016/j.conbuildmat.2020.121699.

[13] T. Ding, J. Xiao, S. Zou, Y. Wang, Hardened properties of layered 3D printed concrete with recycled sand, Cement Concr. Compos. 113 (2020) 103724, https://doi.org/10.1016/j.cemconcomp.2020.103724.

[14] J. Xiao, S. Zou, Y. Yu, Y. Wang, T. Ding, Y. Zhu, J. Yu, S. Li, Z. Duan, Y. Wu, L. Li, 3D recycled mortar printing: system development, process design, material properties and on-site printing, J. Build. Eng. 32 (2020) 101779, https://doi.org/10.1016/j.jobe.2020.101779.

[15] G.H.A. Ting, Y.W.D. Tay, Y. Qian, M.J. Tan, Utilization of recycled glass for 3D concrete printing: rheological and mechanical properties, J. Mater. Cycles Waste Manag. 21 (2019) 994–1003, https://doi.org/10.1007/s10163-019-00857-x.

[16] P. Sikora, E. Horszczaruk, K. Skoczylas, T. Rucinska, Thermal properties of cement mortars containing waste glass aggregate and nanosilica, Procedia Engineering 196 (2017) 159–166, https://doi.org/10.1016/j.proeng.2017.07.186.

[17] A. Alani, J. MacMullen, O. Telik, Z.Y. Zhang, Investigation into the thermal performance of recycled glass screed for construction purposes, Construct. Build. Mater. 29 (2012) 527–532, https://doi.org/10.1016/j.conbuildmat.2011.07.020.

[18] S.-Y. Chung, M. Abd Elrahman, P. Sikora, T. Rucinska, E. Horszczaruk, D. Stephan, Evaluation of the effects of crushed and expanded waste glass aggregates on the material properties of lightweight concrete using image-based approaches, Materials 10 (2017), https://doi.org/10.3390/ma10121354.

[19] M. Mohammad, E. Masad, T. Seers, S.G. Al-Ghamdi, High-performance light-weight concrete for 3D printing, in: F.P. Bos, S.S. Lucas, R.J.M. Wolfs, T.A.M. Salet (Eds.), Second RILEM International Conference on Concrete and Digital Fabrication, Springer International Publishing, Cham, 2020, pp. 459–467.

[20] V. Markin, V.N. Nerella, C. Schröfl, G. Guseynova, V. Mechtcherine, Material design and performance evaluation of foam concrete for digital fabrication, Materials 12 (2019), https://doi.org/10.3390/ma12152433.

[21] A.V. Rahul, M. Santhanam, Evaluating the printability of concretes containing lightweight coarse aggregates, Cement Concr. Compos. 109 (2020) 103570, https://doi.org/10.1016/j.cemconcomp.2020.103570.

[22] L. Wang, H. Jiang, Z. Li, G. Ma, Mechanical behaviors of 3D printed lightweight concrete structure with hollow section, Archiv.Civ.Mech.Eng 20 (2020), https://doi.org/10.1007/s43452-020-00017-1.

[23] H. Zhou, A.L. Brooks, D. Hanna, B. Salarieh, Thermal and mechanical properties of cementitious composites for additive construction of energy-saving habitats Cleveland, Ohio Earth and Space, American Society of Civil Engineers, Reston, VA, 2018, pp. 600–611 11152018.

[24] H. Aglan, S. Shebl, M. Morsy, M. Calhoun, H. Harding, M. Ahmad, Strength and toughness improvement of cement binders using expandable thermoplastic microspheres, Construct. Build. Mater. 23 (2009) 2856–2861, https://doi.org/10.1016/j.conbuildmat.2009.02.031.

[25] A.L. Brooks, H. Zhou, D. Hanna, Comparative study of the mechanical and thermal properties of lightweight cementitious composites, Construct. Build. Mater. 159 (2018) 316–328, https://doi.org/10.1016/j.conbuildmat.2017.10.102.

[26] Y.W.D. Tay, Y. Qian, M.J. Tan, Printability region for 3D concrete printing using slump and slump flow test, Compos. B Eng. 174 (2019) 106968, https://doi.org/10.1016/j.compositesb.2019.106968.

[27] K. Federowicz, M. Kaszyńska, A. Zieliński, M. Hoffmann, Effect of curing methods on shrinkage development in 3D-printed concrete, Materials 13 (2020), https://doi.org/10.3390/ma13112590.

[28] En 196-1, Methods of Testing Cement - Part 1: Determination of Strength, 2016.

[29] En 1015-3, Methods of Test for Mortar for Masonry - Part 3: Determination of Consistence of Fresh Mortar (By Flow Table), 2006.

[30] O. Wünsch, Experimentelle bestimmung binghamscher stoffparameter, Rheol. Acta 29 (1990) 163–169, https://doi.org/10.1007/BF01332383.

[31] En 196-3, Methods of Testing Cement - Part 3: Determination of Setting Times and Soundness, 2016.

[32] M. Haist, J. Link, D. Nicia, S. Leinitz, C. Baumert, T. von Bronk, D. Cotardo, M. Eslami Pirharati, S. Fataei, H. Garrecht, C. Gehlen, I. Hauschildt, I. Ivanova, S. Jesinghausen, C. Klein, H.-W. Krauss, L. Lohaus, D. Lowke, O. Mazanec, S. Pawelczyk, U. Pott, N.W. Radebe, J.J. Riedmiller, H.-J. Schmid, W. Schmidt, E. Secrieru, D. Stephan, M. Thiedeitz, M. Wilhelm, V. Mechtcherine, Interlaboratory study on rheological properties of cement pastes and reference substances: comparability of measurements performed with different rheometers and measurement geometries, Mater. Struct. 53 (2020), https://doi.org/10.1617/s11527-020-01477-w.

[33] F. Celik, H. Canakci, An investigation of rheological properties of cement-based grout mixed with rice husk ash (RHA), Construct. Build. Mater. 91 (2015) 187–194, https://doi.org/10.1016/j.conbuildmat.2015.05.025.

[34] J. Peng, D. Deng, Z. Liu, Q. Yuan, T. Ye, Rheological models for fresh cement asphalt paste, Construct. Build. Mater. 71 (2014) 254–262, https://doi.org/10.1016/j.conbuildmat.2014.08.031.

[35] M. Chougan, S.H. Ghaffar, P. Sikora, S.-Y. Chung, T. Rucinska, D. Stephan, A. Albar, M.R. Swash, Investigation of additive incorporation on rheological, microstructural and mechanical properties of 3D printable alkali-activated materials, Mater. Des. (2021) 109574, https://doi.org/10.1016/j.matdes.2021.109574.

[36] M. Chougan, E. Marotta, F.R. Lamastra, F. Vivio, G. Montesperelli, U. Ianniruberto, A. Bianco, A systematic study on EN-998-2 premixed mortars modified with graphene-based materials, Construct. Build. Mater. 227 (2019) 116701, https://doi.org/10.1016/j.conbuildmat.2019.116701.

[37] M. Chougan, E. Marotta, F.R. Lamastra, F. Vivio, G. Montesperelli, U. Ianniruberto, S. Hamidreza Ghaffar, M.J. Al-kheetan, A. Bianco, High performance cementitious nanocomposites: the effectiveness of nano-Graphite (nG), Construct. Build. Mater. 259 (2020) 119687, https://doi.org/10.1016/j.conbuildmat.2020.119687.

[38] Z. Tan, S.A. Bernal, J.L. Provis, Reproducible mini-slump test procedure for measuring the yield stress of cementitious pastes, Mater. Struct. 50 (2017) 235, https://doi.org/10.1617/s11527-017-1103-x.

[39] M. Chougan, S. Hamidreza Ghaffar, M. Jahanzat, A. Albar, N. Mujaddedi, R. Swash, The influence of nano-additives in strengthening mechanical performance of 3D printed multi-binder geopolymer composites, Construct. Build. Mater. 250 (2020) 118928, https://doi.org/10.1016/j.conbuildmat.2020.118928.

[40] ISO 22007-2, Plastics — Determination of Thermal Conductivity and Thermal Diffusivity — Part 2: Transient Plane Heat Source (Hot Disc) Method, 2015.

[41] H. Alghamdi, S.A.O. Nair, N. Neithalath, Insights into material design, extrusion rheology, and properties of 3D-printable alkali-activated fly ash-based binders, Mater. Des. 167 (2019) 107634, https://doi.org/10.1016/j.matdes.2019.107634.

[42] A. Bhowmick, S. Ghosh, Effect of Synthesizing Parameters on Workability and Compressive Strength of Fly Ash Based Geopolymer Mortar, 2012, pp. 168–177, https://doi.org/10.6088/ijcser.201203013016.

[43] M. Al-Majidi, A. Lampropoulos, A. Cundy, Effect of Alkaline Activator, Water, Superplasticiser and Slag Contents on the Compressive Strength and Workability of Slag-Fly Ash Based Geopolymer Mortar Cured under Ambient Temperature, 2016, https://doi.org/10.5281/zenodo.1112069.

[44] R. Choudhary, R. Gupta, R. Nagar, Impact on fresh, mechanical, and microstructural properties of high strength self-compacting concrete by marble cutting slurry waste, fly ash, and silica fume, Construct. Build. Mater. 239 (2020) 117888, https://doi.org/10.1016/j.conbuildmat.2019.117888.

[45] D. Youness, A. Mechaymech, R. Al Wardany, Flow assessment and development towards sustainable self-consolidating concrete using blended basalt and limestone-cement systems, J. Clean. Prod. 283 (2021) 124582, https://doi.org/10.1016/j.jclepro.2020.124582.

[46] Y. Liu, L. Li, H. Liu, M. Zhang, A. Liu, L. Liu, L. Tang, G. Wang, S. Zhou, Hollow polymeric microsphere-filled silicone-modified epoxy as an internally insulated material for composite cross-arm applications, Compos. Sci. Technol. 200 (2020) 108418, https://doi.org/10.1016/j.compscitech.2020.108418.

[47] G.D. Stefanou, C. Larsinos, Influence of mixing water on the setting time of concrete, Int. J. Cem. Compos. Lightweight Concr. 3 (1981) 45–48, https://doi.org/10.1016/0262-5075(81)90022-1.

[48] N. Tamanna, R. Tuladhar, N. Sivakugan, Performance of recycled waste glass sand as partial replacement of sand in concrete, Construct. Build. Mater. 239 (2020) 117804, https://doi.org/10.1016/j.conbuildmat.2019.117804.

[49] M. Chen, L. Li, Y. Zheng, P. Zhao, L. Lu, X. Cheng, Rheological and mechanical properties of admixtures modified 3D printing sulphoaluminate cementitious materials, Construct. Build. Mater. 189 (2018) 601–611, https://doi.org/10.1016/j.conbuildmat.2018.09.037.

[50] R.D. Hooton, Geiker, M. Brandl, L.N. Thrane, L.F. Nielsen, On the effect of coarse aggregate fraction and shape on the rheological properties of self-compacting concrete, Cem. Concr. Aggregates 24 (2002) 3, https://doi.org/10.1520/CCA10484J.

[51] S.T. Erdoğan, N.S. Martys, C.F. Ferraris, D.W. Fowler, Influence of the shape and roughness of inclusions on the rheological properties of a cementitious suspension, Cement Concr. Compos. 30 (2008) 393–402, https://doi.org/10.1016/j.cemconcomp.2008.01.003.

[52] P. Krause, Thermal Conductivity of the Curing Concrete, Architecture Civil Engineering Environment, 2007, pp. 67–74.

[53] I. Asadi, P. Shafigh, Z.F.B. Abu Hassan, N.B. Mahyuddin, Thermal conductivity of concrete – a review, J. Build. Eng. 20 (2018) 81–93, https://doi.org/10.1016/j.jobe.2018.07.002.

[54] A.A. Jhatial, W.I. Goh, S. Sohu, N. Mohamad, Thermo-mechanical properties of various densities of foamed concrete incorporating polypropylene fibres, Arabian J. Sci. Eng. 45 (2020) 8171–8186, https://doi.org/10.1007/s13369-020-04657-6.

[55] J. Strzałkowski, P. Sikora, S.-Y. Chung, M. Abd Elrahman, Thermal performance of building envelopes with structural layers of the same density: lightweight aggregate concrete versus foamed concrete, Build. Environ. 196 (2021) 107799, https://doi.org/10.1016/j.buildenv.2021.107799.

[56] T.T. Le, S.A. Austin, S. Lim, R.A. Buswell, R. Law, A.G.F. Gibb, T. Thorpe, Hardened properties of high-performance printing concrete, Cement Concr. Res. 42 (2012) 558–566, https://doi.org/10.1016/j.cemconres.2011.12.003.

[57] A.R. Arunothayan, B. Nematollahi, R. Ranade, S.H. Bong, J.G. Sanjayan, K.H. Khayat, Fiber orientation effects on ultra-high performance concrete formed by 3D printing, Cement Concr. Res. 143 (2021) 106384, https://doi.org/10.1016/j.cemconres.2021.106384.

[58] T. Hirsch, T. Dorn, C. Ehm, D. Stephan, Comparison of printable inorganic binders - key properties for 3D printable materials, in: F.P. Bos, S.S. Lucas, R.J.M. Wolfs, T.A.M. Salet (Eds.), Second RILEM International Conference on Concrete and Digital

Fabrication, Springer International Publishing, Cham, 2020, pp. 53–63.

[59] G. Ma, J. Zhang, L. Wang, Z. Li, J. Sun, Mechanical characterization of 3D printed anisotropic cementitious material by the electromechanical transducer, Smart Mater. Struct. 27 (2018) 75036, https://doi.org/10.1088/1361-665X/aac789.

[60] L. Pham, G. Lu, P. Tran, Influences of printing pattern on mechanical performance of three-dimensional-printed fiber-reinforced concrete, 3D Print. Addit. Manuf. (2020), https://doi.org/10.1089/3dp.2020.0172.

[61] Z.Z. Ismail, E.A. Al-Hashmi, Recycling of waste glass as a partial replacement for fine aggregate in concrete, Waste Manag. 29 (2009) 655–659, https://doi.org/10.1016/j.wasman.2008.08.012.

[62] H. Du, K.H. Tan, Concrete with recycled glass as fine aggregates, ACI Mater. J. (2014) 47–58.

[63] R. Polat, M.M. Yadollahi, A.E. Sagsoz, S. Arasan, The correlation between aggregate shape and compressive strength of concrete: digital image processing approach, Int. J. Struct. Civ. Eng. Res. (2013) 63–80.

[64] V. Corinaldesi, A. Nardinocchi, J. Donnini, Reuse of recycled glass in mortar manufacturing, European Journal of Environmental and Civil Engineering 20 (2016) s140–s151, https://doi.org/10.1080/19648189.2016.1246695.

[65] J.R. Wright, C. Cartwright, D. Fura, F. Rajabipour, Fresh and hardened properties of concrete incorporating recycled glass as 100% sand replacement, J. Mater. Civ. Eng. 26 (2014) 4014073, https://doi.org/10.1061/(ASCE)MT.1943-5533.0000979.

[66] P. Spiesz, S. Rouvas, H.J.H. Brouwers, Utilization of waste glass in translucent and photocatalytic concrete, Construct. Build. Mater. 128 (2016) 436–448, https://doi.org/10.1016/j.conbuildmat.2016.10.063.

[67] A. Mardani-Aghabaglou, M. Tuyan, K. Ramyar, Mechanical and durability performance of concrete incorporating fine recycled concrete and glass aggregates, Mater. Struct. 48 (2015) 2629–2640, https://doi.org/10.1617/s11527-014-0342-3.

[68] K. Skoczylas, T. Rucińska, Influence of grain shape of waste glass aggregate on the properties of cement mortar, J. Ecol. Eng. 21 (2020) 148–159, https://doi.org/10.12911/22998993/112975.

[69] K. Skoczylas, T. Rucińska, The effects of waste glass cullets and nanosilica on the long-term properties of cement mortars, E3S Web Conf. 49 (2018) 102, https://doi.org/10.1051/e3sconf/20184900102.

[70] B. Taha, G. Nounu, Utilizing waste recycled glass as sand/cement replacement in concrete, J. Mater. Civ. Eng. 21 (2009) 709–721, https://doi.org/10.1061/(ASCE)0899-1561(2009)21:12(709).

[71] Federal Highway Administration, User Guidelines for Byproduct and Secondary Use Materials in Pavement Construction; FHWA-RD-97-148, Federal Highway Administration, Washington, DC, USA, 2008.

[72] E. Harrison, A. Berenjian, M. Seifan, Recycling of waste glass as aggregate in cement-based materials, Environmental Science and Ecotechnology 4 (2020) 100064, https://doi.org/10.1016/j.ese.2020.100064.

[73] L. Yujing, Z. Wenhua, W. Fan, W. Peipei, Z. Weizhao, Y. Fenghao, Static mechanical properties and mechanism of C200 ultra-high performance concrete (UHPC) containing coarse aggregates, Sci. Eng. Compos. Mater. 27 (2020) 186–195, https://doi.org/10.1515/secm-2020-0018.

[74] J. de Brito, R. Kurda, P. Raposeiro da Silva, Can we truly predict the compressive strength of concrete without knowing the properties of aggregates?, Appl. Sci. 8 (2018) 1095, https://doi.org/10.3390/app8071095.

[75] F. Yang, H. Li, G. Zhao, P. Guo, W. Li, Mechanical performance and durability evaluation of sandstone concrete, Advances in Materials Science and Engineering 2020 (2020) 1–10, https://doi.org/10.1155/2020/2417496.

[76] En 206-1, Concrete. Specification, Performance, Production and Conformity, 2013.

[77] M. Elshahawi, A. Hückler, M. Schlaich, Infra lightweight concrete: a decade of investigation (a review), Struct. Concr. (2020), https://doi.org/10.1002/suco.202000206.

[78] K.-C. Thienel, T. Haller, N. Beuntner, Lightweight concrete-from basics to innovations, Materials 13 (2020), https://doi.org/10.3390/ma13051120.

[79] M. Kupiński, K. Stobieniecka, K. Skowera, Influence of lightweight fillers on the performance of cement-based skim coat, SAE 12 (2020) 5–11, https://doi.org/10.30540/sae-2020-001.